nature photonics

Article

https://doi.org/10.1038/s41566-026-01958-4

Enhanced inverse Compton scattering via spontaneous focusing induced by a coated plasma mirror

Received: 10 November 2025

Accepted: 8 June 2026

Published online: 23 July 2026

Check for updates

Xichen Hu[1,2,7], Mingyang Zhu[1,7], Pengpei Xie[3], Bingjun Li[3], Huitong Zhai[1], Bingzhan Shi[1], Hui Zeng[1], Tianbing Wang[3], Yifei Li[2] ✉, Jinguang Wang[2], Wenchao Yan[1,4], Jie Feng[1,4], Yanfei Li[3], Xin Lu[2,5,6] & Liming Chen[1,4] ✉

Efficient generation of high-energy γ-rays from laser–electron interactions is crucial for advancing nuclear photonics and strong-field quantum electrodynamics. However, the energy-conversion efficiency of plasma-mirror-based all-optical inverse Compton scattering has been fundamentally constrained by the limited overlap between the reflected laser pulse and the wakefield-accelerated electron beam. Here we experimentally demonstrate a coated plasma mirror that spontaneously focuses the reflected pulse, which substantially enhances the local field intensity and strongly drives nonlinear multiphoton inverse Compton scattering. Experiments show that the coating improves the laser-to-radiation energy-conversion efficiency by nearly an order of magnitude compared with uncoated mirrors, at the level of 10^{-4}–10^{-3}, with photon energies extending from tens to hundreds of megaelectronvolts. This simple yet robust approach overcomes the intrinsic energy-utilization limit of plasma-mirror inverse Compton scattering and offers a scalable route towards compact, high-brightness, γ-ray sources for tabletop, strong-field quantum electrodynamics studies and nuclear photonics applications.

Inverse Compton scattering (ICS) is a key process for producing and exploiting high-energy radiation. It provides a unique platform for validating strong-field quantum electrodynamics phenomena, including the radiation reaction[1,2], Schwinger field strength measurements[3] and nonlinear multiphoton processes[4,5]. These investigations are critical for revealing the mysteries of extreme astrophysical environments, such as magnetars and γ-ray bursts[6–8]. Concurrently, ICS is an efficient and reliable way to produce high-brightness, megaelectronvolt to giga-electronvolt photon sources[9,10], with transformative applications spanning nuclear physics[11,12], materials science[13,14], medical imaging[15,16] and inspection technologies[17]. However, the energy-conversion efficiency of ICS has long remained a limiting factor that hinders the realization of these applications.

Advances in laser wakefield acceleration (LWFA) have enabled compact, all-optical ICS sources by intrinsically synchronizing ultra-intense laser pulses (10^{18}–10^{22} W cm^{-2}) with laser-driven femtosecond electron beams[18,19]. Two all-optical experimental configurations dominate: dual-laser collisions and single-laser plasma-mirror (PM)

[1]State Key Laboratory of Dark Matter Physics, Key Laboratory for Laser Plasmas (MoE), School of Physics and Astronomy, Shanghai Jiao Tong University, Shanghai, China. [2]Beijing National Laboratory of Condensed Matter Physics, Institute of Physics, Chinese Academy of Sciences, Beijing, China. [3]Department of Nuclear Science and Technology, School of Energy and Power Engineering, Xi'an Jiaotong University, Xi'an, China. [4]IFSA Collaborative Innovation Center, Shanghai Jiao Tong University, Shanghai, China. [5]School of Physical Sciences, University of the Chinese Academy of Sciences, Beijing, China. [6]Songshan Lake Materials Laboratory, Dongguan, Guangdong, China. [7]These authors contributed equally: Xichen Hu, Mingyang Zhu. ✉e-mail: yflx@iphy.ac.cn; lmchen@sjtu.edu.cn

https://doi.org/10.1038/s41566-026-01958-4

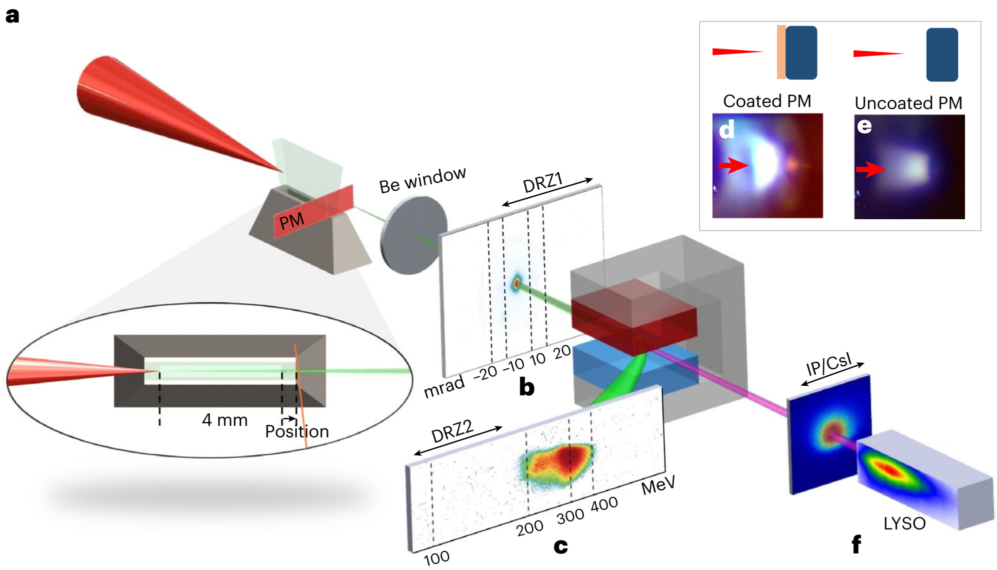

Fig. 1 | Experimental set-up. a, Schematic of the all-optical nonlinear Compton scattering experiment. Inset: top view of the nozzle and PM slightly tilted. We define the PM position as the distance along the axis from the PM surface to the nozzle rear edge (zero point). Negative values correspond to the PM being outside the nozzle. **b**, Typical angular distribution of the electron beam. **c**, Electron energy spectrum. The colour scale indicates the charge density. **d**,**e**, Side-view images of plasma self-emission perpendicular to the laser propagation direction at the target and captured by a visible-light CCD for a coated PM (**d**) and an uncoated PM (**e**). **f**, A CsI scintillation screen or IPs record the radiation profile and photon number distribution. A pixelated cuboid LYSO scintillator serves as a calorimeter to measure the energy of the radiation beam.

reflections. The dual-laser approach has achieved notable advances, with high-order multiphoton scattering[4,5,20] and radiation reaction effects[1,2] propelling it into the quantum electrodynamics regime, as it benefits from the high laser intensities of focused laser pulses[21,22]. In this geometry, multiphoton scattering generates photons from tens of megaelectronvolts to giga-electronvolts from high-energy light sources[23]. This approach offers advantages including radiation purity, flexible control over beam properties and efficient use of colliding pulses. Nevertheless, as a light source, it suffers from limited stability and reliability due to stringent spatio-temporal synchronization challenges on micrometre–femtosecond scales, and its overall laser-to-radiation energy-conversion efficiency typically remains as low as 10^{-6}–10^{-5}.

These constraints have driven the development of single-laser ICS schemes based on PMs[24]. Experiments have confirmed their feasibility[9,25,26] and demonstrated their ability to produce photons with energies reaching the giga-electronvolt scale[27,28]. The intrinsic self-alignment of this geometry removes synchronization constraints while enhancing stability, reliability and repeatability as a light source, which are critical for dynamic imaging. Precursors include static imaging and computed tomography[9,14,16]. However, PM-based ICS provides fewer adjustable degrees of freedom, namely polarization[29], vortices[12] and laser intensity. Moreover, the reflected pulse size typically exceeds both the focal spot and the electron-beam size, as it originates at the LWFA exit. Therefore, electrons interact only with a fraction of the local field of the laser pulse, which severely limits the utilization of the laser energy. Tailored PMs with focusing structures have been proposed to address this mismatch[30–32], but their implementation demands precise optical design, shot-to-shot spatial alignment and control of LWFA instabilities, which reduce the collision probability and increase the risk of laser damage. Evidently, improving the energy-conversion efficiency in PM-based ICS remains challenging.

This Article investigates the enhancement of all-optical ICS in the strongly nonlinear regime due to the use of coated PMs that spontaneously form a focusing structure that strengthens the reflected laser intensity $a_i = eE_i/m_e\omega_l c$, where e is the charge on an electron, E_i is the local field intensity at the electron position, m_e is the mass of an electron, ω_l is the laser angular frequency and c is the speed of light. This self-generated focusing increases a_i from 2.9 to 4.2, thus inducing a sixfold amplification of the photon yield under 100-TW laser power. The associated multiphoton effects extend the critical photon energy from 26 MeV to 39 MeV. At 400 TW, the conversion efficiency approaches 10^{-3}, and the coated PM raises the critical photon energy to 65 MeV. This approach is designed to promote laser utilization, thus enabling nonlinear high-order multiphoton scattering. This new pathway overcomes the long-standing efficiency limitations of PM-based ICS.

Results

Baseline experimental conditions for LWFA

The experiments were carried out with a laser that delivered 2.5 J of energy at the focus with an *f* number of 16.7 and a pulse duration of 28 fs (full-width at half-maximum, FWHM). The normalized vector potential $a_0 = eE_0/m_e\omega_l c \approx 2.14$, where E_0 is the peak field strength of the laser. As shown in Fig. 1a, LWFA was driven by the laser with a gas mixture comprising 1% nitrogen-doped helium from a 4-mm nozzle. The single-shot electron beams had energies ranging from 200 MeV to 400 MeV with an average energy of ~256 MeV (Fig. 1c) and divergence angle of 5.5 mrad (FWHM; Fig. 1b). Particle-in-cell (PIC) simulations (Methods) of the LWFA yielded electron energies that closely matched the experimental measurements (Supplementary Fig. 1), thus laying the groundwork for simulations of the ICS process. As the radiation background, betatron radiation[33] generated from LWFA exhibited a critical energy of 9.5 keV with total photon yield ~2.15×10^5 (Supplementary Fig. 2).

The laser beam exiting the gas medium reflected from a PM and subsequently interacted with the self-aligned counter-propagating electron beam. The PM was either an uncoated 1-mm-thick fused-silica plate or the same substrate carrying a 2-μm-thick loose ZnS overlayer (Methods). The profile and energy spectrum of γ-rays were measured with imaging plates (IPs) and pixelated cerium-doped lutetium yttrium oxyorthosilicate arrays (Ce:LYSO)[34] (Methods). The absence of betatron radiation signals at the LYSO detectors (Fig. 2j) stemmed from the sufficiently low photon energies (Supplementary Fig. 2b) and counts

 https://doi.org/10.1038/s41566-026-01958-4

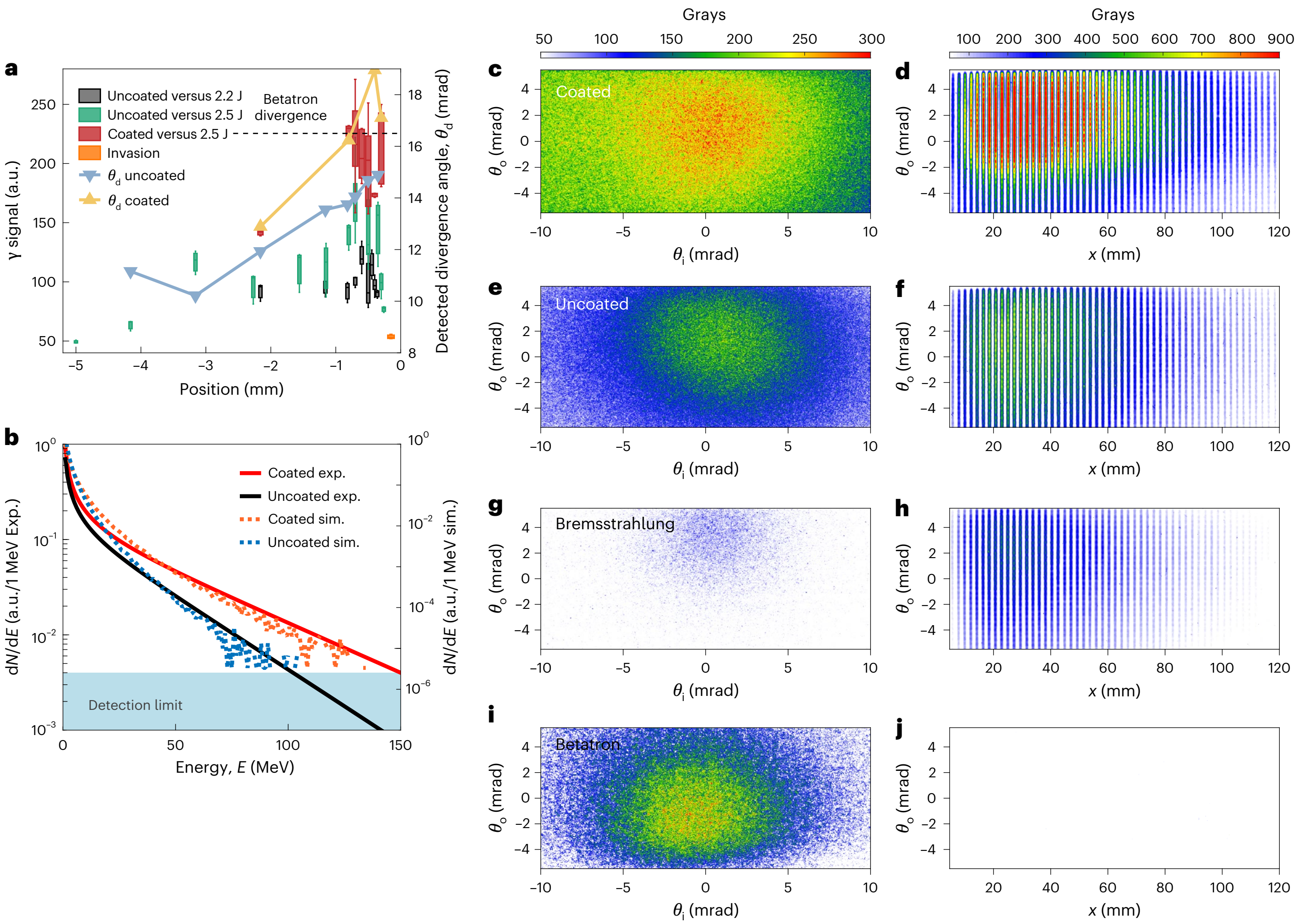

Fig. 2 | Comparison of experimental results. a, Box plots of the radiation signal intensity versus PM position during the experiment. The orange box indicates the case in which the PM intrudes into the gas flow, thereby disturbing it. Each box plot is based on eight technical replicates (laser shots) acquired under identical experimental conditions at the same position but with different PM areas. The box plots show the median, and the box spans the 25th to 75th percentiles (Q1 and Q3). Whiskers extend to the most extreme data points within 1.5 × interquartile range. No outliers were observed. The line plots are the FWHM divergence angles θ_d at several representative positions. The dashed line denotes the experimental FWHM divergence of the betatron radiation (16.8 mrad). **b**, Experimental (solid lines) and simulated (dashed lines) ICS photon spectra. **c**–**j**, Representative radiation spots recorded on IPs and corresponding luminescence distributions on the LYSO detector: radiation spots (**c**) and luminescence distribution (**d**) for a coated PM at −500 µm, radiation spots (**e**) and luminescence distribution (**f**) for an uncoated PM at −500 µm, radiation spots (**g**) and luminescence distribution (**h**) for an uncoated PM at −3,000 µm, and radiation spots (**i**) and luminescence distribution (**j**) for pure betatron radiation without a PM. *N*, photon numbers; θ_i, in-plane angle formed by the incident and reflected rays; θ_o, out-of-plane angle; *x*, luminescence position of the LYSO crystal in the in-plane direction; exp., experimental; sim., simulated.

(Fig. 2i), so that material absorption prevented the development of electron–positron (e^-e^+) pairs. The transmittance of betatron radiation was less than 3.3% for 1-mm SiO_2. The yield was so low that there was almost no betatron radiation signal at the IP and LYSO under the PM configurations, which reduced the interference with the ICS signal.

Confirmation of ICS

First, we confirmed the occurrence of ICS by varying the position of the uncoated PM, as shown in Fig. 2a. The IP signal increased as we moved the PM closer to the nozzle rear edge, peaking between 300 µm and 600 µm. Concurrently, the radiation divergence angle broadened on the IP (Fig. 2a,e,g). The detected photon energy on LYSO rose from that shown in Fig. 2h to that in Fig. 2f. This behaviour is consistent with nonlinear ICS theory, in which shorter distances result in a higher electron–laser interaction strength a_i for ideal beam divergence of a_i/γ (ref. 35), where γ is the Lorentz factor of the relativistic electrons. By contrast, the bremsstrahlung theory of electron beams predicts a nearly constant radiation energy with only a slight reduction in divergence angle at shorter distances, in contradiction with our experimental trends. Moreover, radiation emitted from laser-heated plasma surfaces typically exhibits photon energies in the few kilo-electronvolts range and a large divergence angle[36], rendering it effectively undetectable by the IP and LYSO. To enhance the distinction, we reduced the laser energy to 2.2 J on spot while maintaining nearly identical electron acceleration conditions. As shown by the grey box plots in Fig. 2a, the signal followed the same trend as at 2.5 J but with reduced maxima, while signals at more distant positions (−1 mm to −2 mm) remained unchanged. This establishes a bremsstrahlung background level of ~100 a.u., beyond which the signals explicitly mark the occurrence of ICS.

Radiation enhancement with a coated PM

Significant enhancement was observed when the PM was replaced with a coated PM with 2.5-J laser power. The signal from the coated cases was generally higher at each location than that from the uncoated ones (Fig. 2a). At a typical position of 500 µm, the coated configuration yielded ~7.9 × 10^7 photons (Fig. 2c), achieving a sixfold increase over the uncoated PM case with 1.3 × 10^7 (Fig. 2e). Correspondingly,

https://doi.org/10.1038/s41566-026-01958-4

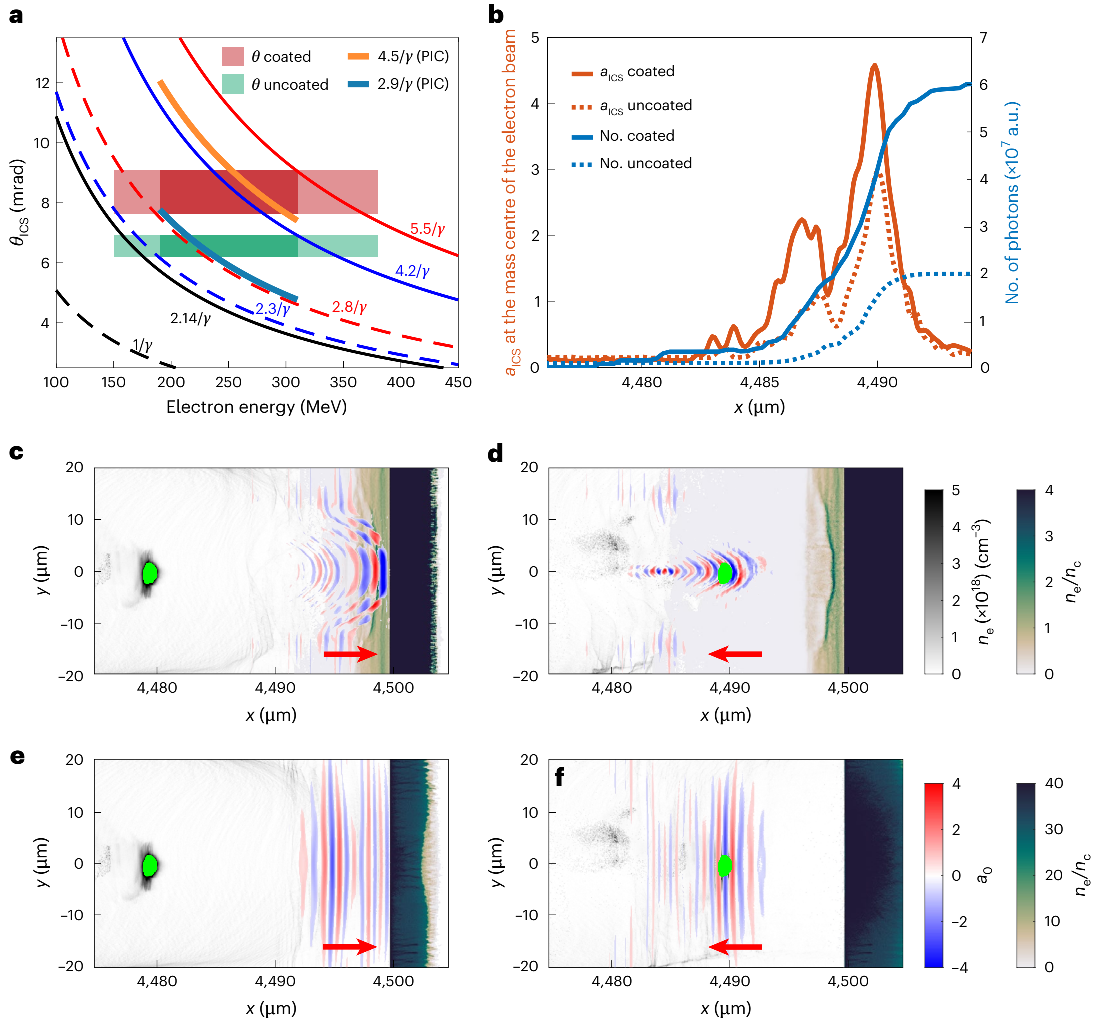

Fig. 3 | Simulations and analysis. a, Comparison of ICS divergence angles. Thin lines in different colours represent a_i/γ. Red and green shaded regions correspond to the ranges of electron energy and θ_{ICS} covered in experiments with coated and uncoated PMs, respectively. Light shading denotes the 95.44% electron coverage range, and dark shading represents the 68.26% range. The coloured, long, solid and dashed lines represent the estimated upper and lower bounds of a_i/γ, respectively, as well as $1/\gamma$. The two bold coloured lines are the a_i/γ curves corresponding to the peak a_i from PIC simulations. **b**, Evolution of the interaction strength a_i experienced by the electron beam centre of mass (noted as a_{ICS}) and the corresponding ICS photon yield from PIC simulations. **c**, PIC-simulated laser penetration into the coated PM. **d**, Collision between the reflected pulse and the electron beam with the coated PM. **e**, PIC-simulated laser penetration into the uncoated PM. **f**, Collision between the reflected pulse and the electron beam with the uncoated PM. Arrows indicate the laser propagation direction, and highlighted green marks represent the electron beam. x, position along the laser propagation direction in the simulation; y, position along the laser polarization direction; n_e, plasma density. The grey colour represents the plasma in the LWFA, and the green colour represents that in the plasma mirror.

the signal on the LYSO (Fig. 2d,f) was longer with the coated PM. The photon spectra in Fig. 2b show that the critical energy $E_{cri} = 39$ MeV and the cutoff energy $E_{cut} = 150$ MeV of ICS radiation obtained by the coated PM were substantially higher than for the uncoated case, which realized $E_{cri} = 26$ MeV and $E_{cut} = 100$ MeV. It is important to note that using the coated PM simultaneously increased the number of photons, radiant energy and divergence angle. However, the contributions to the enhancement must be identified. First, the thickness of the coat was only a few micrometres, so that it could not appreciably enhance the bremsstrahlung when the accelerated electron beam traversed the PM. Hence, we assumed that the three quantities were unchanged. Second, although the coating could have slightly modified the bremsstrahlung produced by laser-heated electrons at the solid surface, such a thin layer cannot account for the pronounced enhancement in the energies of the photons to tens or hundreds of megaelectronvolts. Therefore, the most plausible explanation is the enhancement of the interaction strength in ICS enabled by the coat of PM.

We evaluated the interaction strength a_i from the radiation divergence angle to investigate the coating-induced laser enhancement (Fig. 3a). For a non-ideal electron beam, the half-angle of the in-plane radiation cone for ICS was estimated as $\theta_{ICS} = \sqrt{\theta_i^2 - \theta_e^2}$ (refs. 20,37), where θ_i and θ_e are half-widths at 1/e of the maximum detected in-plane radiative divergence and $\theta_i = \theta_d/2\sqrt{\ln 2}$. A clear separation in θ_{ICS} between coated and uncoated cases is evident for the predominant electron energy spectrum (95.44% (2σ) and 68.26% (1σ)) and the divergence angles derived from PM positions within −0.3 mm to −1 mm, as indicated by the rectangular regions in Fig. 3a. In both cases, the divergence angles deviated from the linear scaling of $1/\gamma$, characteristic of nonlinear ICS, thus linking the divergence angle to the interaction strength as $\theta_{ICS} \approx a_i/\gamma$. On estimating a_i/γ, we found that the lower limit of the ICS interaction strength for uncoated PMs coincides with the vacuum laser focal intensity $a_0 = 2.14$, achievable in LWFA through laser self-focusing. For the 1σ energy range of dominant electrons, a_i spans 2.3–4.2 for uncoated PM but 2.8–5.5 for a coated PM, indicating that the interaction strength increases away from a_0. This enhancement

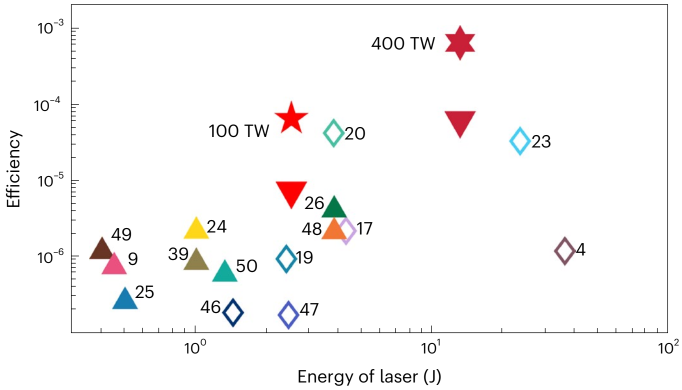

Fig. 4 | Energy-conversion efficiency. Comparison of laser-to-radiation energy-conversion efficiencies. Diamonds represent dual-laser schemes[4,17,19,20,23,46,47], and triangles represent PM schemes[9,24–26,39,48–50]. The inverted red triangle denotes the 100-TW uncoated result from this work and the pentagram denotes the coated case. The deeper-red hexagram corresponds to our 400-TW coated case, and the inverted deeper-red triangle to the uncoated case.

cannot be explained solely by laser self-focusing in LWFA, implying that the coating introduces another focusing mechanism.

PIC simulations reveal the interaction dynamics and clarify the coating-induced enhancement mechanism. In the uncoated PM configuration, when the laser exits the gas target with a peak intensity of $a_0 \approx 2.8$, the SiO_2 surface is ionized by the pulse front, generating a far overcritical plasma density ($n_c = m_e\omega_l^2/4\pi e^2$) with a tiny scale length such that there is almost specular reflection of the pulse (Fig. 3f). By contrast, the coated PM configuration produces a lower plasma density upon laser-front ionization, enabling partial penetration of the pulse into the plasma. Owing to the stronger ponderomotive force and radiation pressure at the centre and the weaker force at the edges, electrons near the axis acquire a larger transverse momentum than those in the wings, which leads to a larger longitudinal momentum and density accumulation, driving the density front deeper on axis than off axis (Supplementary Fig. 4). This results in a shock-like density front with a concave profile that is deeper at the centre and shallower towards the periphery[38–41] (Fig. 3c). According to relativistic transparency, the effective critical density is $n_c' = \gamma n_c$, which scales with intensity through $\gamma = \left(1 + a_0^2/2\right)^{1/2}$ (ref. 42). Consequently, a higher a_0 shifts the reflection condition to higher density, so the beam centre is reflected later and deeper than the wings. The wavefront thus bends to produce a focused reflection with an intensity boost near the focal spot[40,43] (Fig. 3d). Experimental side-view observations corroborate this picture. As shown in Fig. 1d,e, the plasma luminescence from the coated PM exhibits pronounced curvature, whereas that from the uncoated PM remains flat.

Examining the consistency between simulations and experiments, we recorded the laser intensity at the centre of mass of the electron beam, that is, the ICS interaction intensity a_i and the number of photons >500 keV at the same moment (Fig. 3b). For the coated PM, a_i increased to 4.5 near the focus, compared with the maximum a_i of 2.9 for the uncoated case, in agreement with the estimate in Fig. 3a. The corresponding lines for $4.5/\gamma$ and $2.9/\gamma$ passed through their respective experimental θ_{ICS} regions. The synchronized increase in photon yield with a_i confirms the effectiveness of the laser enhancement (Fig. 3b). On the other hand, the electron beam exhibited a divergence angle of 12.5 mrad in the simulation, whereas the photon divergence angles were 15.2 mrad for the coated case and 14.3 mrad for the uncoated case. Calculations give divergences θ_{ICS} of 8.6 mrad and 6.9 mrad, respectively, which fall within their respective experimental ranges in Fig. 3a. Furthermore, the simulated photon energy spectra also agree closely with the experimental observations, as illustrated in Fig. 2b. The cutoff energy of the uncoated case was around 100 MeV, whereas the coated configuration achieved a cutoff energy of ~130 MeV. These results indicate that the coating enhances the interaction strength via spontaneous focusing, as in the simulations, leading to a simultaneous increase in both the photon yield and energy.

The enhancement of the ICS photon energy and yield improved the laser energy-conversion efficiency. First, under the same laser-energy input, the coated PM refocused the laser before ICS, thereby minimizing the non-interacting regions and increasing the number of scattering events. This advance breaks through the long-standing inefficiency bottleneck of PM-based schemes to boost the ICS photon yield. Second, the focused laser drives stronger nonlinear interactions. The elevated laser photon density enhances the probability of higher-order multiphoton ICS processes within the coherence length[44], thus improving the energy transferred per scattering event. For an electron with an energy of 300 MeV, the photon energy of ICS predicted by linear scattering theory $E_\gamma \approx 2\gamma^2(1 - \cos\phi_{coll})E_L$ is ~2 MeV, which is far below the experimental observations, where the collision angle $\phi_{coll} \approx \pi$ and E_L is the laser photon energy. This discrepancy necessitates the consideration of nonlinear scattering theory. According to the relation $E_\gamma = n\frac{2\gamma^2(1-\cos\phi_{coll})E_L}{1+(a_i^2/2)+\gamma^2\theta^2}$ (ref. 45), the fundamental photon energies for the coated and uncoated configurations are estimated to be 0.2 MeV and 0.4 MeV, respectively. The corresponding critical photon energies reach the 200th and 65th harmonics of the fundamental, respectively, which demonstrates the pronounced effect of multiphoton scattering induced by the coating.

Conversion efficiency

Calculations based on typical LWFA-driven all-optical ICS experiments (Fig. 4) show that the coated scheme achieves a conversion efficiency higher by one order of magnitude than comparable laser systems. In the tens of terawatt regime, the PM schemes already surpass dual-laser configurations with efficiencies of ~10^{-6} (ref. 24). However, as the laser energy and power increase to several joules and a few hundred terawatts, the limited interaction region inherent to the PM scheme becomes increasingly restrictive, whereas the dual-laser configuration can provide more tightly focused colliding beams[4,20], gradually surpassing it in efficiency. By employing a coated PM, we modified the laser focusing characteristics in the PM scheme, thereby enabling the effective utilization of laser energy that would otherwise not contribute to the collision. As a result, the conversion efficiency improved from 7.4×10^{-6} to 6.5×10^{-5}, as illustrated in Fig. 4.

A higher laser energy is expected to result in a higher energy-conversion efficiency. We operated the petawatt (PW) laser system in 400-TW mode, which increased the laser focal energy to 12 J. Our experimental results demonstrate a significant enhancement of ICS (Supplementary Fig. 3). With the coated scheme, the critical photon energy reached 60 MeV, with a cutoff energy of ~400 MeV and a photon yield of 8×10^9 per shot (Supplementary Fig. 3), far exceeding the performance of the uncoated configuration, which had a critical energy of 29 MeV and a photon yield of 8×10^8. The energy-conversion efficiency with the coated PM improved to ~6×10^{-4}, again representing nearly an order of magnitude enhancement. This advance can be attributed, on the one hand, to the increase in electron energy up to 1 GeV with a charge of ~200 pC (Supplementary Fig. 1), and on the other hand, to the facilitation of the formation of a focusing structure enabled by such an intense laser. PIC simulations indicate that the peak interaction strength increased from 9 to nearly 13 (Supplementary Fig. 3). It is foreseeable that, under PW operating conditions, both the interaction strength and the conversion efficiency can be further enhanced.

Discussion

Our scheme expands the possibilities for ICS experiments based on PMs. The experiment demonstrates that the ICS source based on the coated PM can simultaneously achieve high photon energy, high yield and notably high-energy-conversion efficiency. This provides strong support for the development of high-energy γ-ray beamlines applicable to the inspection of thick metallic components, high-density materials and other demanding scenarios[10], thus making it suitable for nuclear physics experiments such as on nuclear resonance fluorescence and nuclear transmutation[12,19]. Moreover, the results indicate that even with moderate laser energy or power, it is still possible to achieve higher interaction intensities through laser refocusing, thus enabling quantum electrodynamics experiments. Interestingly, the experiment effectively creates a unique environment characterized by a high-density plasma, high-energy electrons, intense electromagnetic fields and strong radiation. Moreover, it offers a new experimental platform for investigating extreme astrophysical scenarios, such as those found in supernovae, pulsars and γ-ray bursts[46–48].

Additionally, this experiment demonstrates a method for modifying laser properties through PM surface design and modification, and it provides insights that may enhance laser-manipulation techniques, such as polarization[25,29], vortex production[49] and flying focus[50] in PM-based ICS experiments. This approach indicates the potential for developing strong-field metamaterial surfaces to control reflected laser characteristics, which is an interesting combination with materials science[51]. It could efficiently overcome the long-standing challenge of the low degree of controllability inherent in PM approaches.

In conclusion, we have introduced a simple and efficient method to overcome the low efficiency bottleneck of PM ICS. We experimentally demonstrated that a coated PM enables spontaneous focusing of the reflected laser pulse, thus markedly enhancing the laser energy-conversion efficiency in the single-beam scheme for ICS. The coating improved conversion efficiency by an order of magnitude at 100 TW and approached 10^{-3} at 400 TW. Nonlinear effects became prominent, with critical photon energies extending from tens to hundreds of megaelectronvolts in a high-order multiphoton process. With the integration of PW lasers and PM surface control, further improvements in both controllability and efficiency are anticipated.

Online content

Any methods, additional references, Nature Portfolio reporting summaries, source data, extended data, supplementary information, acknowledgements, peer review information; details of author contributions and competing interests; and statements of data and code availability are available at https://doi.org/10.1038/s41566-026-01958-4.

References

1. Cole, J. M. et al. Experimental evidence of radiation reaction in the collision of a high-intensity laser pulse with a laser-wakefield accelerated electron beam. *Phys. Rev. X* **8**, 011020 (2018).
2. Poder, K. et al. Experimental signatures of the quantum nature of radiation reaction in the field of an ultraintense laser. *Phys. Rev. X* **8**, 031004 (2018).
3. Bulanov, S. S. et al. On the design of experiments to study extreme field limits. *AIP Conf. Proc.* **1507**, 825–830 (2012).
4. Sarri, G. et al. Ultrahigh brilliance multi-MeV gamma-ray beams from nonlinear relativistic Thomson scattering. *Phys. Rev. Lett.* **113**, 224801 (2014).
5. Khrennikov, K. et al. Tunable all-optical quasimonochromatic Thomson X-ray source in the nonlinear regime. *Phys. Rev. Lett.* **114**, 195003 (2015).
6. Qu, Y. & Zhang, B. Coherent inverse Compton scattering in fast radio bursts revisited. *Astrophys. J.* **972**, 124 (2024).
7. Mernier, F. et al. Discovery of inverse-Compton X-ray emission and estimate of the volume-averaged magnetic field in a galaxy group. *Mon. Not. R. Astron. Soc.* **524**, 4939–4949 (2023).
8. Xie, Y. et al. Origin of FRB-associated X-ray burst: QED magnetic reconnection. *Sci. Bull.* **68**, 1857–1861 (2023).
9. Ma, Y. et al. Region-of-interest micro-focus computed tomography based on an all-optical inverse Compton scattering source. *Matter Radiat. Extremes* **5**, 064401 (2020).
10. Chaulagain, U. et al. ELI gammatron beamline: a dawn of ultrafast hard X-ray science. *Photonics* **9**, 853 (2022).
11. Shvyd'ko, Y. et al. Resonant X-ray excitation of the nuclear clock isomer 45Sc. *Nature* **622**, 471–475 (2023).
12. Lu, Z.-W. et al. Angular momentum resolved inelastic electron scattering for nuclear giant resonances. *Phys. Rev. Lett.* **134**, 052501 (2025).
13. Singh, M., Tondon, A., Sandhu, B. S. & Singh, B. Compton scattering geometry: a tool to study radiation interaction characteristics of rare earth compounds doped in low-*Z* organic compound. *Radiochim. Acta* **111**, 367–386 (2023).
14. Karimi, S. et al. CT results using an inverse Compton X-ray source. In *Proc. Anomaly Detection and Imaging with X-rays (ADIX) VIII* Vol. 12531 (eds Ashok, A. et al.) 1253102 (SPIE, 2023).
15. McAnespie, C. A. et al. High-dose femtosecond-scale gamma-ray beams for radiobiological applications. *Phys. Med. Biol.* **67**, 085010 (2022).
16. Panetta, D. et al. Numerical simulation of novel concept 4D cardiac microtomography for small rodents based on all-optical Thomson scattering X-ray sources. *Sci. Rep.* **9**, 8439 (2019).
17. Chen, S. et al. Shielded radiography with a laser-driven MeV-energy X-ray source. *Nucl. Instrum. Methods Phys. Res. Sect. B* **366**, 217–223 (2016).
18. Corde, S. et al. Femtosecond X rays from laser-plasma accelerators. *Rev. Mod. Phys.* **85**, 1–48 (2013).
19. Chen, S. et al. MeV-energy X rays from inverse Compton scattering with laser-wakefield accelerated electrons. *Phys. Rev. Lett.* **110**, 155003 (2013).
20. Yan, W. et al. High-order multiphoton Thomson scattering. *Nat. Photonics* **11**, 514–520 (2017).
21. Danson, C. N. et al. Petawatt and exawatt class lasers worldwide. *High Power Laser Sci. Eng* **7**, e54 (2019).
22. Li, Y. et al. High-intensity lasers and research activities in China. *High Power Laser Sci. Eng* **13**, e12 (2025).
23. Mirzaie, M. et al. All-optical nonlinear Compton scattering performed with a multi-petawatt laser. *Nat. Photonics* **18**, 1212–1217 (2024).
24. Ta Phuoc, K. et al. All-optical Compton gamma-ray source. *Nat. Photonics* **6**, 308–311 (2012).
25. Ma, Y. et al. Compact polarized X-ray source based on all-optical inverse Compton scattering. *Phys. Rev. Appl.* **19**, 014073 (2023).
26. Yu, C. et al. Ultrahigh brilliance quasi-monochromatic MeV γ-rays based on self-synchronized all-optical Compton scattering. *Sci. Rep.* **6**, 29518 (2016).
27. Gerstmayr, E. et al. High brightness multi-MeV photon source driven by a petawatt-scale laser wakefield accelerator. Preprint at https://arxiv.org/abs/2506.23718 (2025).
28. Matheron, A. et al. Compton photons at the GeV scale from self-aligned collisions with a plasma mirror. Preprint at https://arxiv.org/abs/2412.19337 (2024).
29. Ma, Q. et al. Production of multioriented polarization for relativistic electron beams via a mutable filter for nonlinear Compton scattering. *Phys. Rev. Appl.* **19**, 014058 (2023).
30. Yu, Q., Gu, Y. J., Zhang, Y., Kong, Q. & Kawata, S. Compact Compton γ-ray source from a spatiotemporal-modulated pulse scattering a high-energy electron beam. *Phys. Plasmas* **31**, 083101 (2024).
31. Feng, J. et al. Intense γ ray generated by refocusing laser pulse on wakefield accelerated electrons. *Phys. Plasmas* **24**, 093110 (2017).

32. Ong, J. F., Seto, K., Berceanu, A. C., Aogaki, S. & Neagu, L. Feasibility studies of an all-optical and compact γ-ray blaster using a 1 PW laser pulse. *Plasma Phys. Control. Fusion* **61**, 084009 (2019).
33. Huang, K. et al. Resonantly enhanced betatron hard X-rays from ionization injected electrons in a laser plasma accelerator. *Sci. Rep.* **6**, 27633 (2016).
34. Behm, K. T. et al. A spectrometer for ultrashort gamma-ray pulses with photon energies greater than 10 MeV. *Rev. Sci. Instrum.* **89**, 113303 (2018).
35. Esarey, E., Ride, S. K. & Sprangle, P. Nonlinear Thomson scattering of intense laser pulses from beams and plasmas. *Phys. Rev. E* **48**, 3003–3021 (1993).
36. Morris, S., Robinson, A. & Ridgers, C. Highly efficient conversion of laser energy to hard X-rays in high-intensity laser–solid simulations. *Phys. Plasmas* **28**, 103304 (2021).
37. Li, Y., Huang, Z., Borland, M. D. & Milton, S. Small-angle Thomson scattering of ultrafast laser pulses for bright, sub-100-fs X-ray radiation. *Phys. Rev. Accel. Beams* **5**, 044701 (2002).
38. Wang, X.-B. et al. Gamma-ray generation from ultraintense laser-irradiated solid targets with preplasma. *High Power Laser Sci. Eng* **8**, e34 (2020).
39. Tsai, H. E. et al. Compact tunable Compton X-ray source from laser-plasma accelerator and plasma mirror. *Phys. Plasmas* **22**, 023106 (2015).
40. Tsai, H.-E. et al. Self-aligning concave relativistic plasma mirror with adjustable focus. *Phys. Plasmas* **24**, 013106 (2017).
41. Chopineau, L. et al. Spatio-temporal characterization of attosecond pulses from plasma mirrors. *Nat. Phys.* **17**, 968–973 (2021).
42. King, M. et al. Perspectives on laser-plasma physics in the relativistic transparency regime. *Eur. Phys. J. A* **59**, 132 (2023).
43. Vincenti, H. Achieving extreme light intensities using optically curved relativistic plasma mirrors. *Phys. Rev. Lett.* **123**, 105001 (2019).
44. Di Piazza, A., Müller, C., Hatsagortsyan, K. Z. & Keitel, C. H. Extremely high-intensity laser interactions with fundamental quantum systems. *Rev. Mod. Phys.* **84**, 1177–1228 (2012).
45. Downer, M. C., Zgadzaj, R., Debus, A., Schramm, U. & Kaluza, M. C. Diagnostics for plasma-based electron accelerators. *Rev. Mod. Phys.* **90**, 035002 (2018).
46. Harding, A. K. Physics in ultra-strong magnetic fields. *Proc. Int. Astron. Union* **16**, 149–161 (2020).
47. Wadiasingh, Z., Baring, M. G., Gonthier, P. L. & Harding, A. K. Resonant inverse Compton scattering spectra from highly magnetized neutron stars. *Astrophys. J.* **854**, 98 (2018).
48. Malu, S. et al. Relativistic inverse Compton scattering of photons from the early Universe. *Sci. Rep.* **7**, 16918 (2017).
49. Taira, Y. Spatial distribution of gamma rays produced by axially symmetric polarized and optical vortex lasers. *Phys. Rev. A* **110**, 043525 (2024).
50. Formanek, M., Ramsey, D., Palastro, J. P. & Di Piazza, A. Radiation reaction enhancement in flying focus pulses. *Phys. Rev. A* **105**, L020203 (2022).
51. Piccardo, M. et al. Trends in relativistic laser–matter interaction: the promises of structured light. *Optica* **12**, 732–752 (2025).

https://doi.org/10.1038/s41566-026-01958-4

Methods

Laser wakefield acceleration

The experiment was performed at the ultrafast X-ray dynamics experimental station of the Synergetic Extreme Condition User Facility at the Institute of Physics, Chinese Academy of Sciences. A linearly polarized 800-nm laser pulse of length 28 fs was focused onto a 4-mm-long supersonic nozzle using an off-axis parabolic mirror with a 3-m focal length ($F\# = 16.7$). Operating in the 100-TW regime, the laser delivered 2.52 J of energy to a near-Gaussian focal spot of width $w_0 = 10.85$ μm, achieving a peak intensity of 9.9×10^{18} W cm^{-2}, corresponding to $a_0 \approx 2.14$. The gas target was a mixture of 99% He and 1% N_2, yielding a plasma density of 4.5×10^{18} cm^{-3}. Electrons and radiation propagated through a 170-cm vacuum section before passing through a 380-μm-thick beryllium window into the ambient atmosphere. In the 400-TW configuration, 12 J of laser energy was effectively delivered to the focal spot. To enhance the efficiency of LWFA, we used helium gas doped with 1% oxygen.

Electron diagnostics

The electron energy spectra generated by LWFA were measured using a magnetic spectrometer, namely a 1.2-T dipole magnet (20 cm in length and 8 cm in width) positioned 202.5 cm downstream from the target. Dispersed electrons were detected 30 cm behind the magnet exit using a DRZ-High scintillator (Gd_2O_2S:Tb). This is where an IP could be attached for charge quantification. Neither detector was exposed to radiation. A secondary DRZ screen was installed at the magnet entrance to monitor the electron-beam position and divergence during measurements, which was removed before performing the radiation diagnostics. The system achieved a detectable energy range spanning 50–1,200 MeV, with an energy resolution of 2 MeV at 400 MeV. The statistical analysis incorporating the incidence positions in front of the magnet of individual shots revealed that the electron energy was relatively stable (Supplementary Fig. 1). The beam had a pointing jitter of 20 mrad while maintaining a charge ranging from 22 pC to 40 pC.

Radiation diagnostics

The radiation passed through the beryllium window and magnet before being recorded by an IP positioned 75 cm downstream of the magnet, which captured its intensity profile. For the betatron radiation energy measurements, a stack of four IPs spaced 5 cm apart resolved the spectrum to reveal a critical energy of ~9.5 keV and a cutoff energy of ~40 keV through spectral deconvolution (Supplementary Fig. 2). The energy of the ICS γ-rays was detected by a pixelated Ce:LYSO scintillator array located 87 cm from the magnet, which was composed of orthogonally alternating $1 \times 1 \times 40$ mm^3 scintillator elements separated by 0.1-mm barium sulfate ($BaSO_4$) reflective spacer layers. The energy spectrum was solved as in an electromagnetic calorimeter, in which γ-rays undergo electromagnetic showers, thus causing the crystal to emit light. The luminescence was collected by a 3-inch lens positioned 18 cm away from the LYSO surface and subsequently imaged onto a 16-bit electron-multiplying charge-coupled device. Using the Monte Carlo code Geant4 and the measured γ-ray profile, the luminescence distribution of monoenergetic photons (1 MeV to 500 MeV) $S(x, E_j)$ within the LYSO detector was simulated so that we could iteratively reconstruct the photon energy spectrum via the synchrotron-like function $\mathrm{d}N/\mathrm{d}E \propto E^{-2/3}\,\mathrm{e}^{-E/E_c}$ and bremsstrahlung e^{-E/E_t} where E is the γ-ray energy, E_t is the characteristic energy of bremsstrahlung and E_c is critical energy of ICS[23,34]. The constraint used to reconstruct the energy spectrum was to minimize the expression $\sigma = [r_i - \Sigma_j S_{ij}(\frac{\mathrm{d}N(E_j)}{\mathrm{d}E})\Delta E_j]$, where r_i is the lineout of the detected signal from LYSO, ΔE_j represents the energy bin used for reconstruction and S_{ij} is the matrix element of the response $S(x, E_j)$ from Geant4.

Plasma mirror

As a control, the uncoated PM had a 1-mm-thick fused-silica substrate with low thermal expansion, a mass density of ~2.2 g cm^{-3} and an SiO_2 formula-unit number density of $\sim 12.7n_c$. The coated PM was prepared by depositing a loose ZnS layer onto the fused-silica surface to an average thickness of 2 μm and an average mass density of ~0.032 g cm^{-3}, which corresponds to a molecular number density of $\sim 0.11n_c$. Although the ZnS layer was not very uniform on the nanometre scale, for a relativistic laser focal spot with a transverse size of several tens of micrometres, it served as a reasonably good approximation of a uniform-density medium, and we adopted it as a simplified model in the PIC simulations.

PIC simulations

The PIC simulations were performed using the open-source code EPOCH. The plasma target was 4.5 mm long. It has 1-mm linear density up- and down-ramps and a plateau electron density of 4.5×10^{18} cm^{-3}. The target was He with 1% N_2 doping, with He fully ionized and N initialized with five pre-ionized outer-shell electrons. A Gaussian laser pulse with width $w_0 = 11$ μm and $a_0 = 2.14$ was focused at 1.5 mm from the front edge. A SiO_2 PM was placed at 4.5 mm. It had a thickness of 1 mm and molecular density of 2.66×10^{22} cm^{-3} (~$12.7n_c$) without pre-ionization. For the coated PM, a 2-μm-thick ZnS layer was initialized as neutral molecules with a molecular number density of $0.1n_c$. It was placed in front of the SiO_2 substrate over 4,498–4,500 μm, without pre-ionization. The simulation box measured 50 m × 100 m (longitudinal distance times transverse distance) with spatial resolution $\Delta x = 2\Delta y = \lambda/20$. The LWFA gas was initialized with 8 pseudo-particles per cell, whereas the PM region had 400 particles per cell.

Data availability

Data supporting the findings of this study are available in the article and Supplementary Information or from the corresponding authors upon reasonable request. Source data are provided with this paper.

Code availability

The custom codes used to produce the results presented in this paper are available from the corresponding authors upon reasonable request.

Acknowledgements

This work was carried out at the ultrafast X-ray dynamics experimental station of the Synergetic Extreme Condition User Facility (http://cstr.cn/31123.02.SECUF.D3). The computations in this paper were run on the π 2.0 cluster supported by the Center for High Performance Computing at Shanghai Jiao Tong University.

Author contributions

L.C. conceived the project. X.H., M.Z., Yifei Li, P.X., B.L., H. Zhai, B.S., H. Zeng and T.W. performed the experiments and collected the data. X.H., M.Z. and P.X. analysed the experimental data and carried out the simulations and analytical calculations. Yifei Li, J.W., W.Y., J.F., X.L. and L.C. provided the experimental platforms, equipment, technical expertise and funding support. X.H. wrote the paper, which was reviewed by Yifei Li, Yanfei Li and L.C.

Funding

L.C. discloses support for the research and publication of this work from the National Key Research and Development Program of China [Grant No. 2025YFF0515002] and the National Natural Science Foundation of China [Grant Nos. 12335016, W2412039 and 11991073]. W.Y. discloses support for the research of this work from the National Key Research and Development Program of China [Grant No. 2025YFF0515002]. J.F. discloses support for the research of this work from the National Natural Science Foundation of China [Grant No. 12305272]. The other authors received no specific funding for this work.

Competing interests

The authors declare no competing interests.

Additional information

Supplementary information The online version contains supplementary material available at https://doi.org/10.1038/s41566-026-01958-4.

Correspondence and requests for materials should be addressed to Yifei Li or Liming Chen.

Peer review information *Nature Photonics* thanks the anonymous reviewers for their contribution to the peer review of this work.